

Quantifying focal mechanism heterogeneity for fault zones in central and southern California

Iain W. Bailey,¹ Yehuda Ben-Zion,¹ Thorsten W. Becker¹ and Matthias Holschneider²

¹Department of Earth Sciences, University of Southern California, Los Angeles, USA. E-mail: iwbailey@usc.edu

²Institute of Mathematics, University of Potsdam, Potsdam, Germany

Accepted 2010 July 19. Received 2010 May 25; in original form 2009 June 2

SUMMARY

We present a statistical analysis of focal mechanism orientations for nine California fault zones with the goal of quantifying variations of fault zone heterogeneity at seismogenic depths. The focal mechanism data are generated from first motion polarities for earthquakes in the time period 1983–2004, magnitude range 0–5, and depth range 0–15 km. Only mechanisms with good quality solutions are used. We define fault zones using 20 km wide rectangles and use summations of normalized potency tensors to describe the distribution of double-couple orientations for each fault zone. Focal mechanism heterogeneity is quantified using two measures computed from the tensors that relate to the scatter in orientations and rotational asymmetry or skewness of the distribution. We illustrate the use of these quantities by showing relative differences in the focal mechanism heterogeneity characteristics for different fault zones. These differences are shown to relate to properties of the fault zone surface traces such that increased scatter correlates with fault trace complexity and rotational asymmetry correlates with the dominant fault trace azimuth. These correlations indicate a link between the long-term evolution of a fault zone over many earthquake cycles and its seismic behaviour over a 20 yr time period. Analysis of the partitioning of San Jacinto fault zone focal mechanisms into different faulting styles further indicates that heterogeneity is dominantly controlled by structural properties of the fault zone, rather than time or magnitude related properties of the seismicity.

Key words: Earthquake dynamics; Earthquake source observations; Seismicity and tectonics; Statistical seismology; Dynamics: seismotectonics; Fractures and faults.

1 INTRODUCTION

Heterogeneity of a fault zone can refer to any departure from a single planar surface within material that has homogeneous mechanical properties. In this study, we focus on quantifying the variation of $0 < M_L \leq 5$ earthquake focal mechanism orientations to better characterize geometrical heterogeneity at seismogenic depths of strike-slip faults in southern California. Geometrical heterogeneity can take many forms, for example, offsets of the fault surface (step-overs), changes in the fault orientation due to kinks or bends, roughness of the fault surface, and overlapping fault segments. Slip across such geometrically heterogeneous surfaces has important implications for the mechanics of individual earthquake ruptures. For example, King & Nábělek (1985) and Wesnousky (2006) showed a tendency for large earthquakes to start and stop close to geometrical irregularities. Dieterich & Smith (2009) showed that slip on a geometrically rough surface leads to a complex stress field around the fault affecting the subsequent distribution of seismicity. Models that simulate seismicity and evolving stress over hundreds of years indicate that fault and stress heterogeneity can act as a tuning parameter for the frequency-size distribution as well as other statistical

properties of the seismicity (e.g. Ben-Zion & Rice 1995; Ben-Zion *et al.* 2003; Zöller *et al.* 2005; Hillers *et al.* 2006, 2007; Bailey & Ben-Zion 2009). Although fault heterogeneity is often considered to be fractal without characteristic length-scales (e.g. Turcotte 1997), previous work (Bailey *et al.* 2009) indicated that the scale of large ~50–250 km fault zones exerts a strong influence on the coseismic strain release characteristics of small earthquakes in southern California. This and other works suggest that large faults or fault zones can be considered as having some distinct length scales, and more diverse heterogeneity than pure self-similarity.

One approach used to quantify geometrical heterogeneity has been to analyse maps of surface fault traces (e.g. Wesnousky 1988; Stirling *et al.* 1996; Ando *et al.* 2009; Wechsler *et al.* 2010). Surface traces are produced by the cumulative displacement over many earthquake cycles, reflecting the long-term strain release within a fault zone. Results of these studies indicate that faults with larger cumulative displacement have smaller amounts of geometrical complexity, implying a gradual evolution of faults towards smoother geometries that is consistent with other multi-disciplinary observations (Ben-Zion & Sammis 2003). A problem associated with the use of fault trace data are that they only provide a 2-D

image of the fault zone at the Earth's surface, where the normal stress is lower and heterogeneity is expected to be higher than at seismogenic depths (e.g. Rockwell & Ben-Zion 2007). Here, we approach this problem by combining fault trace with earthquake catalogue data, which sample throughout the upper ~ 20 km of the crust in a well-instrumented region such as California. A single earthquake focal mechanism represented by a double-couple (DC) orientation describes the earthquake rupture in terms of an axis of maximum compression, an axis of maximum extension and an axis of zero net strain (e.g. Kagan 1991). Assuming that most earthquakes in a fault zone occur on the pre-existing fault surfaces of a fault zone, variation of DC orientations within the zone describe changes in fault orientation related to geometrical heterogeneity of the faults.

To quantify heterogeneity for a set of DC orientations we use an approach based on summation of normalized potency tensors (e.g. Kostrov 1974; Bailey *et al.* 2009). A summation of potency tensors is proportional to the total seismic strain release for the earthquake population (e.g. Kostrov 1974; Amelung & King 1997; Sipkin & Silver 2003), while normalizing before summation allows us to concentrate on statistical properties of the orientation of strain release (e.g. Fischer & Jordan 1991; Frohlich & Apperson 1992; Bailey *et al.* 2009). The summations provide two quantities that describe the heterogeneity: one related to the amount of scatter in orientations and one related to the rotational asymmetry of this scatter. Previous studies that quantify the heterogeneity of a focal mechanism population are based on the distribution of angles for the minimum rotation between every pair of DC orientations (e.g. Kagan 1990; Hardebeck 2006) and do not target individual fault zones. Although those studies describe the scatter in DC orientations as a distribution, hence providing more detail, they do not describe the asymmetry in DC orientations which we show to be an important characteristic in the description of focal mechanism heterogeneity for a given fault zone.

Where Bailey *et al.* (2009) showed that patterns of earthquake strain release can be length-scale dependent, this study addresses the quantification of heterogeneity levels for specific targeted fault zones. We combine a higher quality subset of focal mechanism data used in that study with additional focal mechanism data for the Parkfield region and a data set of surface traces to investigate nine strike-slip fault zones in southern and central California. The previously employed methods based on potency tensor summations are expanded to analyse and interpret the focal mechanism data in terms of fault zone heterogeneity rather than overall coseismic strain. As suggested by Bailey *et al.* (2009), we find that we can distinguish fault zones by the level and type of heterogeneity in focal mechanism orientations. Furthermore, by comparing the focal mechanism heterogeneity with properties of the surface trace azimuths we show that geometrical properties at depth relate to those at the surface. We find a correlation between the focal mechanism scatter and the scatter in fault trace azimuths, along with a correlation between the focal mechanism asymmetry and the dominant surface trace azimuth. The first correlation indicates that geometrical heterogeneity at the surface persists to depth, and that geometrical features related to the long-term properties of strain release are reflected at a ~ 20 yr time scale. The second correlation implies that long-term strike-slip motion in a direction not aligned with plate motion leads to secondary components of reverse or normal faulting, as expected from the direction of misalignment.

Numerical simulations in Appendix C show that our focal mechanism heterogeneity results may be explained by the level of partitioning into different faulting styles within a fault zone. We therefore

investigate the partitioning into the different faulting styles for the four fault zones with the largest number of data. For the San Jacinto fault zone, which has the most data, we investigate the partitioning as a function of hypocentre location, time and magnitude. We find that the location of the earthquakes exert the strongest control on the partitioning and that there is little indication of a strong magnitude-based or temporal effect. Many of the focal mechanism data are clustered in space, and the clusters of seismicity are themselves heterogeneous with different levels of partitioning. The applicability of focal mechanism results to an entire fault zone therefore depends on how representative those clusters are for the fault zone as a whole. Since large sections of the San Andreas Fault that has the largest cumulative slip are relatively straight and produce little low magnitude seismicity, the differences among the examined fault zones are likely to be larger than those shown by our analysis of the limited available data.

The major issues addressed in this paper are (i) how to quantify heterogeneity from focal mechanism data, (ii) the different characteristics of heterogeneity in different fault zones, (iii) the relations between focal mechanism heterogeneity and observations of the fault zone at the surface and (iv) the partitioning of strain release within an individual fault zone. The remainder of the paper is organized into four sections centred around these major issues and Appendices that provide more detail on the data and the quantities used. In Section 2, we describe the fault trace and focal mechanism data. In Section 3, we discuss the employed methods for quantifying fault trace heterogeneity, focal mechanism heterogeneity and the partitioning of focal mechanism data into different faulting styles. The results of quantifying heterogeneity for all fault zones are given in Section 4, as well as results for the partitioning of faulting styles as a function of space, time and magnitude within the San Jacinto fault zone data. A discussion of each of the major results is given in Section 5.

2 DATA

2.1 Fault trace data

Digitized fault trace data used in this study are defined by the USGS quaternary fault map (California Geological Survey & U.S. Geological Survey 2010). In this data set faults with Quaternary activity are discretized into segments of varying length with approximate accuracy of 140 m. We select nine different fault zones from southern and central California (Fig. 1) that are strike-slip dominated and have earthquake data available in the vicinity. We concentrate on strike-slip fault zones to minimize the effect of dipping faults on extrapolating surface properties to those at depth. Seven of the zones relate to large, well-known faults in southern California: the San Andreas (SAF; represented by four different sections), the San Jacinto, the Elsinore and the Garlock faults. The other two zones are part of the Eastern California Shear Zone (ECSZ), and are both collections of smaller faults that contain the surface ruptures of the 1992 $M_W = 6.2$ Joshua Tree and $M_W = 7.3$ Landers earthquakes (ECSZ 1), and the 1999 $M_W = 7.1$ Hector Mine earthquake (ECSZ 2).

To define the fault zone boundaries, we first approximate each fault zone by a great circle arc connecting two coordinates, then incorporate all data with perpendicular distance to the arcs ≤ 10 km. The coordinates (given in Appendix A) are chosen such that by eye the arcs overlay the appropriate fault traces, removing parts where there is no seismicity. For ECSZ 1 and ECSZ 2, several minor faults are incorporated and the choice of coordinates is based more on the

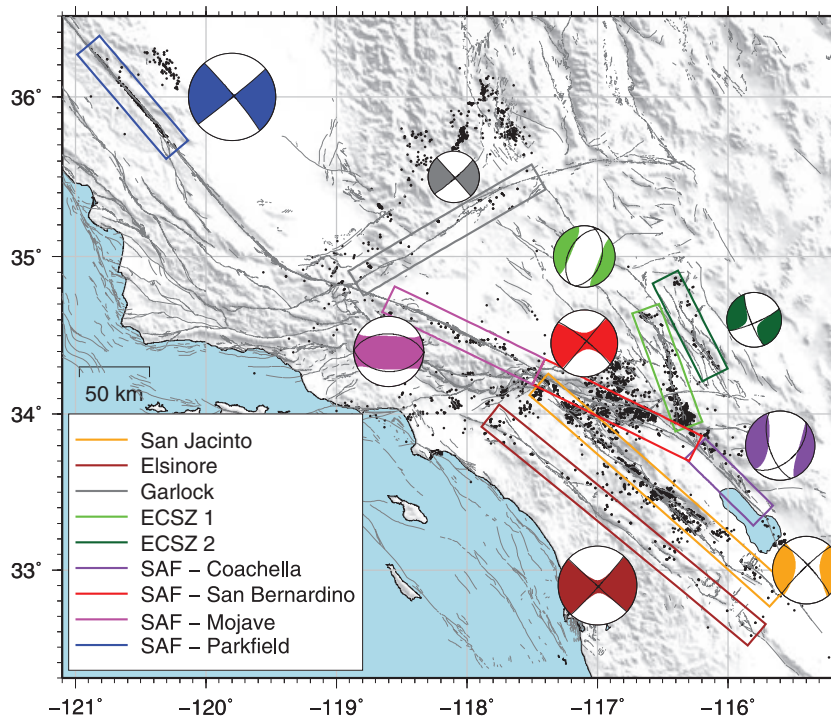


Figure 1. Map of southern and central California showing epicentre locations of earthquake focal mechanisms (black dots), boundaries of the nine fault zones (colored lines), and summed focal mechanism orientations for each fault zone. The summation results are shown by beachballs, where white regions indicate the orientation of compression, colored regions indicate extension, black lines indicate the double-couple part of the result, and the radii are scaled by $1 - \Delta V_{NORM}$ (eq. 3) for relative comparison.

traces of the large earthquake surface ruptures. In some cases, our choice of zones leads to the inclusion of small amounts of data from nearby fault zones and some data being incorporated into multiple zones. However, we have found that other methods of selection which better separate fault zones lead to similar results (Bailey 2009) while being more complicated to implement and reproduce. The choice of 10 km on either side of the great circle arc is roughly equal to two thirds of the depth extent of the seismogenic zone, and allows for some flexibility with respect to earthquake location errors and dipping faults while providing an adequate number of focal mechanism data for analysis.

Uncertainties and sample biases within the fault data are likely to be present due to variable resolution of the mapping across the region and the inherent subjectivity involved during the mapping process. We have tried to minimize the influence of these factors by using a single up-to-date data source but it is very difficult to account for many of these uncertainties. Since we do not make any decisions that we see to accentuate the variable uncertainty within the fault data, we assume that it has a negligible influence on our results.

2.2 Focal mechanism data

We assume that a point-source DC representation is adequate for $0 < M_L \leq 5$ earthquakes in southern California. The DC solutions used in this study are computed from first motion polarities using the program *HASH* (Hardebeck & Shearer 2002). The program computes a set of acceptable fault plane solutions that fit the phase data within some predefined misfit threshold and returns the preferred solution as the average of this set. The uncertainty of the solution is quantified by the range of acceptable solutions. Effects of uncertainty in the hypocentre location on the solution are incorporated by recomputing acceptable solutions using a number

of velocity models. We use only A and B quality mechanisms from the catalogues for which the root mean square angular difference in acceptable solutions (FPU) is $\leq 35^\circ$, 60 per cent of acceptable solutions are within 30° of the preferred solution (i.e. $PROB = 0.6$), the misfit of the fault plane inversion is less than 20 per cent, and the ratio describing how well stations sample the focal sphere ($STDR$) is ≥ 0.4 . In Appendix B, we compare heterogeneity results based on the A and B quality data with those based on relaxed quality constraints. The lower quality constraints allow the use of more data, but changes in the heterogeneity can largely be explained by increased uncertainty in those data. The advantage of using quality restrictions based on a number of factors (FPU , $PROB$ and $STDR$) is that distributions of uncertainties will be similar for multiple data sets, and relative differences are more likely to indicate changes in natural heterogeneity.

For all fault zones except the Parkfield section of the SAF, we use focal mechanisms from the catalogue of Hardebeck *et al.* (2005), available via the Southern California Earthquake Data Center. This covers the time period January 1984–December 2003. We reassign the hypocentre locations using the LSH (1.12) relocated catalogue of Lin *et al.* (2007). For the Parkfield section of the SAF, we use the catalogue generated for the study of Thurber *et al.* (2006). This catalogue covers the period May 1979–August 2005, and is limited to a rectangular region surrounding Parkfield. For both catalogues, we restrict magnitude to $0 < M_L \leq 5$ and depth to $z \leq 15$ km.

3 METHODS

3.1 Fault trace heterogeneity

Fault trace segments are assigned to a given fault zone if both vertices of the segment are within 10 km of the great circle arc

used to define that zone. We quantify geometrical characteristics of mapped fault traces using the distribution of azimuths weighted by length of the segments. We choose this method rather than number of stepovers per unit length (as in Wesnousky 1988; Stirling *et al.* 1996), since it is less subjective given the digital data, and less sensitive to uncertainties in mapping of fault terminations (see also Wechsler *et al.* 2010).

We extract the length and azimuth of each segment k to define a 2-D vector $x_i^{(k)}$. Since the fault trace segments are axial quantities with 180° periodicity, the distribution of all $x_i^{(k)}$ can be described by a scatter matrix (Mardia & Jupp 1999, p. 165)

$$\hat{T}_{ij} = \frac{1}{\sum_k L_k^2} \sum_k x_i^{(k)} x_j^{(k)}, \quad (1)$$

where L_k is the length of the k th of M segments for the fault zone. The scatter matrix is analogous to an inertia tensor about a single origin for particles of equal weight at different positions given by $x_i^{(1)}, \dots, x_i^{(M)}$. The axis about which there is least moment describes the principle direction of the fault trace population. We denote the maximum and minimum eigenvalues of \hat{T}_{ij} as τ_2 and τ_1 , respectively, and the corresponding eigenvectors as \hat{u}_i and \hat{v}_i . In this notation, \hat{u}_i corresponds to the principle direction and τ_1/τ_2 , which is constrained to the range $0 \leq \tau_1/\tau_2 \leq 1.0$, describes the degree of scatter or dispersion away from the principle direction. We use \hat{u}_i and τ_1/τ_2 to quantify the dominant direction and overall variation of the fault trace populations, respectively. The dispersion or variation of geometrical fault zone heterogeneities was shown by numerous theoretical studies to strongly affect the dynamics of earthquakes associated with the fault zone (see e.g. fig. 24 of Ben-Zion (2008) and related material).

Our method of quantifying complexity makes no distinction between smooth and sudden changes in fault direction that would have different implications for rupture mechanics. We also weight each segment of the fault trace based only on length, regardless of the amount of slip or slip rate that are not provided in the data set. Despite these limitations, τ_1/τ_2 represents a simple measure of geometrical variability within the fault zone, and values are consistent with a visual assessment of the fault maps as well as other measures such as the circular standard deviation (Fisher 1993, p.37).

3.2 Focal mechanism heterogeneity

We describe the orientation of a focal mechanism using a normalized potency tensor \hat{P}_{ij} satisfying $\sqrt{\hat{P}_{ij}\hat{P}_{ij}} = 1$. The unit norm mechanism tensor \hat{P}_{ij} gives the orientation of the coseismic strain drop that generates seismic radiation and is related directly to the strike, dip and rake of the DC fault plane solution (equations are given in Appendix A of Bailey *et al.* 2009). The final (static) potency tensor of an earthquake is given by $P_{ij} = \frac{1}{\sqrt{2}} P_0 \hat{P}_{ij}$ where P_0 is the scalar potency, and the final seismic moment tensor is $M_{ij} = \sum_{k,l} c_{ijkl} P_{kl}$ where c_{ijkl} is the tensor of elastic constants in the source region (Ben-Zion 2008). The orientation of a DC has three degrees of freedom and as such \hat{P}_{ij} is symmetric, has zero trace, zero determinant and unit Euclidean norm. The advantage of this representation over other representations (see Kagan 2005) is that one DC orientation is unambiguously defined by only one tensor. By using the normalized potency/moment tensor, we disregard magnitude information associated with the earthquakes and concentrate on the orientation rather than the amount of strain release. A comparison of results for analysis methods based on the potency and normalized potency tensors is given by Bailey *et al.* (2009).

We describe the combined orientation properties for a population of N tensors using the summed source mechanism tensor (e.g. Kostrov 1974; Bailey *et al.* 2009),

$$E_{ij} = \sum_k \hat{P}_{ij}^{(k)}, \quad (2)$$

which is symmetric and has zero trace due to the DC nature of $\hat{P}_{ij}^{(k)}$, leaving five degrees of freedom. If $\hat{P}_{ij}^{(k)}$ was the same for all k , that is, a summation of homogeneously oriented DCs, then $E_{ij} = (N/\sqrt{2})\hat{P}_{ij}$ for which the Euclidean norm is $\sqrt{E_{ij}E_{ij}} = N$ and the intermediate eigenvalue is $\lambda_2 = 0$. For E_{ij} computed from non-homogeneous orientations, the two degrees of freedom that quantify departure from this homogeneous result relate to heterogeneity of orientations in the population. A value of the norm of E_{ij} smaller than N indicates scatter in the DC orientations, and a non-zero value of λ_2 indicates rotational asymmetry in that scatter.

We quantify the tensor norm related measure of heterogeneity using the metric

$$\Delta r_{NORM} = 1 - \frac{\sqrt{E_{ij}E_{ij}}}{N}, \quad (3)$$

where $0 \leq \Delta r_{NORM} \leq 1$. This quantifies the inconsistency in orientations of the population ($1 - \Delta r_{NORM}$ is termed the seismic consistency by Frohlich & Apperson 1992). It is zero when all DCs have the same orientation, unity when all values of $P_{ij}^{(k)}$ cancel each other out, and $\sim 1/\sqrt{N}$ for a summation of uniformly random orientations.

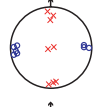
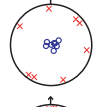
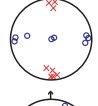
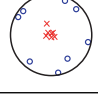
For a DC tensor, the value of λ_2 is always zero, signifying that there is no net strain in the direction of the intermediate strain axis (B-axis). For E_{ij} the net strain must be re-stated in terms of number of events, and a non-zero λ_2 results from an asymmetric distribution in B-axis orientations. We quantify this measure of heterogeneity using

$$r_{CLVD} = \frac{\sqrt{6}}{2} \frac{\lambda_2}{\sqrt{E_{ij}E_{ij}}}, \quad (4)$$

where the *CLVD* subscript refers to the compensated linear vector dipole component that is typically used to describe the non-DC part of a deviatoric tensor (Knopoff & Randall 1970; Julian *et al.* 1998). The range of possible values is $-0.5 \leq r_{CLVD} \leq 0.5$, where $r_{CLVD} = 0$ for a pure DC. Positive or negative values of r_{CLVD} from a summation of normalized DC tensors imply a difference between the variation of P and T axes orientations, as summarized with examples in Table 1 using the convention that extension is positive and compression is negative. If $r_{CLVD} = 0$ and Δr_{NORM} is small, the DC orientations must all be closely aligned. If $r_{CLVD} = 0$ and Δr_{NORM} is large, the DC orientations are likely to be heterogeneous but the P and T axes vary in the same manner, such that deformation in the direction of the intermediate axis is cancelled out. For summation over N uniformly random DC orientations, the probability distribution for r_{CLVD} has the form $\cos[\pi r_{CLVD}]$ when $N \geq 3$ (Bailey *et al.* 2009). The quantities r_{CLVD} and Δr_{NORM} are related to general focal mechanism scatter and the relative contribution of different faulting styles by numerical simulations in Appendix C.

Distributions of rotation angles (e.g. Kagan 1990; Hardebeck 2006) and the associated axes of rotation (Kagan 2009) provide a more complete description of focal mechanism heterogeneity, but there are two advantages of using quantities based on the summation of source mechanism tensors: first the fault plane ambiguity has no impact on how we measure the difference between mechanisms, and second it is unnecessary to run computations for all pairs in a

Table 1. The CLVD component of E_{ij} interpreted in terms of mixing of strike-slip, reverse and normal faulting styles, assuming that one of the principle axes of E_{ij} is vertical. Four cases of a potential result with a CLVD component are shown in the third column using a convention that extension is positive and compression is negative. The associated faulting styles and example distributions of P-axes (red crosses) and T-Axes (blue circles) are shown in the fourth and fifth columns.

r_{CLVD}	Vertical Strain	E_{ij} Appearance	Faulting Styles	P and T axis distribution
$r_{CLVD} < 0$	Compression		Strike-slip + Normal	
	Extension		Reverse, variable strike	
$r_{CLVD} > 0$	Extension		Strike-slip + Reverse	
	Compression		Normal, variable strike	

population which leads to a rapid (N^2) increase in computational time with number of data. In Appendix D, we show that Δr_{NORM} is proportional to the mean of the minimum rotation angles between all pairs of DC orientations, and r_{CLVD} relates to the distribution of axes about which those rotations occur.

3.3 Strain partitioning

The partitioning of the focal mechanism data into different deformation styles provides insight into the underlying processes that lead to non-zero values of Δr_{NORM} and r_{CLVD} . We estimate the homogeneous part of E_{ij} , or the dominant direction for the population, by computing the orientation of the DC component of E_{ij}

$$\hat{E}_{ij}^{DC} = \frac{1}{\sqrt{2}}(t_i t_j - p_i p_j), \quad (5)$$

where t_i and p_i denote the eigenvectors corresponding to the maximum and minimum eigenvalues of E_{ij} , λ_3 and λ_1 , respectively (taking extension to be positive). We can define six end-member cases of DC orientation for a given E_{ij} using

$$\begin{aligned} \hat{E}_{ij}^A &= \hat{E}_{ij}^{DC}, \\ \hat{E}_{ij}^B &= \frac{1}{\sqrt{2}}(b_i b_j - p_i p_j), \\ \hat{E}_{ij}^C &= \frac{1}{\sqrt{2}}(t_i t_j - b_i b_j), \\ \hat{E}_{ij}^D &= \frac{1}{\sqrt{2}}(p_i p_j - b_i b_j), \\ \hat{E}_{ij}^E &= \frac{1}{\sqrt{2}}(b_i b_j - t_i t_j), \\ \hat{E}_{ij}^F &= \frac{1}{\sqrt{2}}(p_i p_j - t_i t_j), \end{aligned} \quad (6)$$

where \hat{E}_{ij}^{DC} is defined in eq. (5) and b_i is the intermediate strain axis of E_{ij} . Larger values of the inner product between two tensors imply greater similarity, and we allocate each $\hat{P}_{ij}^{(k)}$ in a fault zone population to one of the six end-member cases based on the largest value of the inner product. \hat{E}_{ij}^B and \hat{E}_{ij}^C share either a P or T axis with the dominant DC orientation \hat{E}_{ij}^A . Assuming that slip occurs in the

direction of maximum shear stress resolved onto a pre-existing fault plane, DC focal mechanisms with these two orientations can result from a loading tensor with principle stress orientations parallel to the P , B and T axes of E_{ij}^A (McKenzie 1969), indicating that loading orientation could be relatively homogeneous. \hat{E}_{ij}^D , \hat{E}_{ij}^E and \hat{E}_{ij}^F do not share either P or T axes with E_{ij} , and any partitioning of focal mechanisms into these directions indicates strong variation in the loading tensor orientation for the population. For the San Jacinto fault zone, which has the most focal mechanism data, we use these end-members to investigate the partitioning as a function of epicentre location, hypocentre depth, magnitude and time.

To better visualize the spatial locations of focal mechanisms from the different partitioning groups, we use a kernel smoothing approach to plot the density of epicentres and density of hypocentre depths along strike. We define a 2-D Gaussian function with standard deviation of 1 km centred on each earthquake location. The density of earthquakes at each point in a grid encompassing the fault zone is then computed as the sum of all Gaussians evaluated at that gridpoint.

4 RESULTS

4.1 Source mechanism summations

We compute E_{ij} for each of the nine focal mechanism populations representing the different fault zones. The results are shown by ‘beachball’ plots that indicate the distribution of compressive and extensive axes in Fig. 2 next to corresponding angular histograms of fault trace azimuths. We find that the distribution of fault traces is quite variable, with some fault zones (e.g. Coachella, Mojave) showing asymmetry. The crossing black lines overlaying the beachballs denote the DC part of the summed tensors \hat{E}_{ij}^{DC} , which in all cases except Coachella, Mojave and ECSZ 1 imply a dominant strike-slip mechanism with orientation that can be reconciled with the distribution of fault trace azimuths. This indicates that the dominant fault structures in the region tend to control the dominant focal mechanism orientation. In the three cases where \hat{E}_{ij}^{DC} is not of strike-slip faulting type, the dominant focal mechanism orientations do not

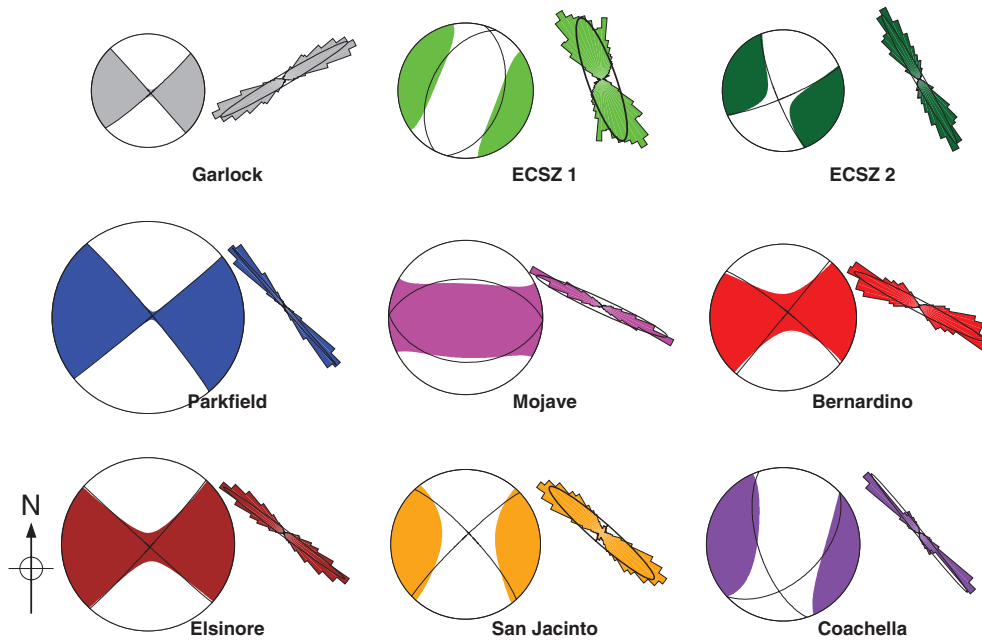


Figure 2. Summed source mechanism tensor E_{ij} results and angular histograms of the fault traces for each of the fault zones. The beachball plots indicate orientations of compression and extension for E_{ij} by white and colored regions, respectively, on an equal-area lower-hemisphere projection. The radius of each beachball is scaled by $1 - \Delta r_{NORM}$ to indicate the relative consistency of orientations. Lines within the beachballs show the double-couple part of the result. The angular histograms are based on computing the total length of the digitized fault trace segments within 5° bins of azimuth which are mirrored to highlight the 180° periodicity. The histogram bins are all normalized by the maximum bin size such that the scale is arbitrary. Ellipses overlaying the histograms represent \hat{u}_i by the orientation of the long axis and the size of τ_1/τ_2 by the short-long axis aspect ratio.

correspond to the surface trace orientations and therefore appear to be sampling more secondary fault structures.

4.2 Focal mechanism heterogeneity

We compute Δr_{NORM} and r_{CLVD} from each of the E_{ij} for the populations shown in Fig. 2. The comparison of values shown in Fig. 3 illustrates the relative heterogeneity of the different fault zones. We perform a bootstrap resampling (Press *et al.* 1992, p. 691) on each of the nine sets of focal mechanisms 10 000 times to compute a range for the values of Δr_{NORM} and r_{CLVD} . The range indicates the robustness of our results that is generally reflective of the number of focal mechanisms in each population. We find no correlation be-

tween the number of data and the values of Δr_{NORM} and r_{CLVD} . The bootstrap errors do not take into account the uncertainties associated with the focal mechanisms that are more difficult to constrain (see Appendix B) and we therefore concentrate on relative differences between fault zones. These relative differences illustrate that there are distinct focal mechanism heterogeneity levels for the nine fault zones.

The Parkfield section of the SAF lies noticeably closer to zero for both measures, indicating more homogeneity than for the other fault zones. For the zones in southern California, values of Δr_{NORM} are in the range 0.2–0.50 with several overlapping error bounds. The different fault zones are better distinguished by values of r_{CLVD} which span close to the entire -0.5 to 0.5 range. This indicates that asymmetry in a population of focal mechanism orientations is fundamental to a description of their heterogeneity. We find that Δr_{NORM} is broadly correlated with $|r_{CLVD}|$ until reaching the most heterogeneous fault zones: Garlock and ECSZ 2. In these two zones (for which there are small numbers of data) we find a high value of Δr_{NORM} and low value of r_{CLVD} due to diverse populations of DC orientations, where a roughly equal number of normal and reverse faulting mechanisms cancel each other out.

4.3 Relationships between fault trace and focal mechanism properties

Fig. 4 shows the relationships between (a) α_u and r_{CLVD} , where α_u is the azimuth from north of \hat{u}_i , and (b) τ_1/τ_2 and Δr_{NORM} . In the case of the Garlock fault zone which is the only dominantly left-lateral fault zone, we subtract 90° from α_u to make it comparable with the other fault zones. The errors bars for α_u correspond to the minimum angular range that includes 50 per cent of the combined fault trace length.

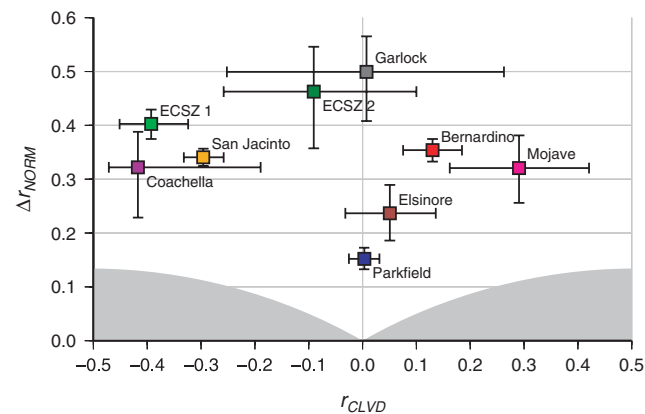


Figure 3. Classification of focal mechanism heterogeneity by Δr_{NORM} and r_{CLVD} for each of the nine fault zones. Error bars indicate the minimum and maximum values of each quantity from bootstrap resampling. Grey regions indicate impossible combinations of the Δr_{NORM} and r_{CLVD} .

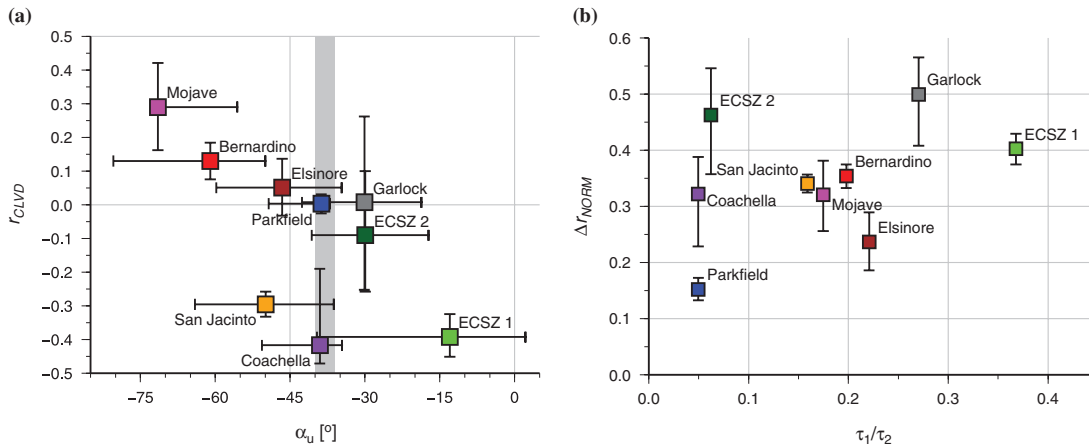


Figure 4. (a) Azimuth of the principle orientation of fault traces α_u versus r_{CLVD} from the source mechanism tensor summation for each of the nine fault zones. The α_u value plotted for the Garlock fault represents the actual value minus 90° . The error bars for α_u correspond to the minimum angular range that includes 50 per cent of the combined fault trace length which is not necessarily symmetric about α_u . Error bars for r_{CLVD} show the minimum and maximum values from bootstrap resampling. The grey bar indicates the range in azimuths of relative plate motion for the region. (b) Dispersion of fault trace orientations τ_1/τ_2 versus Δr_{NORM} for the fault zones. Error bars for Δr_{NORM} show the minimum and maximum values from bootstrap resampling.

We find a negative correlation between α_u and r_{CLVD} with a Pearson correlation coefficient of $r_P = -0.67$ and Spearman Rank correlation coefficient of $r_S = -0.60$ (Fig. 4a). This indicates a relation between the dominant orientation of the fault zone and asymmetry in the distribution of focal mechanism orientations. For reference, we also show the range in azimuths of local relative plate motion between the Pacific and North American plates for the region as a grey bar from -40° to -36° (using NUVEL-1A, DeMets *et al.* 1994). Although the plate motion azimuth corresponds to α_u for the two fault zones where $r_{CLVD} \approx 0$, an azimuth of $\sim -45^\circ$ would better separate the positive from negative values of r_{CLVD} .

Fig. 4(b) shows a positive correlation of $r_P = 0.38$ and $r_S = 0.47$ between τ_1/τ_2 and Δr_{NORM} . This indicates a correlation between the complexity of faults measured at the surface and the scatter in focal mechanism orientations, though it is not strong. The three fault zones with the smallest number of focal mechanism data (Coachella, ECSZ 2 and Garlock) show relatively higher values of Δr_{NORM} , but the bootstrap resampling and our simulations in Appendix C indicate that Δr_{NORM} is not as well constrained when $N \lesssim 100$. Furthermore, the zone ECSZ 2 sits on the edge of the region and seismic network, and is likely to have the least resolution in fault data and most biases in focal mechanism orientation. If we were to consider this as an outlier and remove it, the value of r_P would improve to 0.64.

Based on a Student's *t*-test, the correlation between τ_1/τ_2 and Δr_{NORM} with all zones is only significant at a 67 per cent confidence level, whereas the correlation between α_u and r_{CLVD} is more significant at a 95 per cent level. However, the assumption of an underlying normal distribution required for this test is not realistic due to the bounded range of the quantities considered and we therefore cannot place too much weight on these significance values. Nevertheless, the correlations presented are similar for a number of different measures of mean direction and deviation described by Fisher (1993).

4.4 Strain partitioning

Fig. 5 displays the partitioning of focal mechanism data into the six deformation styles defined by eq. (6). We show results only

for the four fault zones where $N > 100$ (San Jacinto, ECSZ 1, San Bernardino and Parkfield). In all regions except the ECSZ 1, we find that the number of data belonging to categories \hat{E}_{ij}^D , \hat{E}_{ij}^E and \hat{E}_{ij}^F is negligible, implying that the principle axes of the deviatoric loading tensor for the fault zones are close in direction to the strike-slip consistent strain axes of \hat{E}_{ij}^A . For the Parkfield section, we find that very few of the focal mechanisms are classified outside of \hat{E}_{ij}^A , implying that only minor variations about the dominant strike-slip sense of deformation exist, as suggested by Thurber *et al.* (2006). The San Jacinto and San Bernardino fault zones have dominant strike-slip components and second-order components consistent with the sign of r_{CLVD} . We also find third-order components that indicate further, non-trivial complexity in the variation of faulting orientations. For these fault zones where \hat{E}_{ij}^A is of strike-slip type, the co-existence of \hat{E}_{ij}^B and \hat{E}_{ij}^C type mechanisms may be explained by strong variations in strike of the dipping faults responding to a similar stress tensor, by spatial and temporal variations in stress acting on similarly oriented dip slip faults, or by a combination of both.

For ECSZ 1, the DC part of E_{ij} has a near-vertical *P*-axis and therefore \hat{E}_{ij}^A and \hat{E}_{ij}^B are both normal faulting styles. The presence of focal mechanisms in both of the normal faulting categories indicates the existence of normal faulting with highly variable strike. Although variation in the strike of dipping faults could generate a CLVD component in E_{ij} (Example 4 in Table 1), the orientation of the CLVD component for ECSZ 1 shows (Fig. 2) that it is generated by a mixing of \hat{E}_{ij}^C strike-slip and \hat{E}_{ij}^A normal faulting mechanisms. The dominant DC direction is of normal faulting type when most of the mapped faults are of right-lateral strike-slip type, which indicates a strong influence of dilational step-overs from the Joshua Tree and Landers ruptures upon their aftershock characteristics, as observed by Felzer & Beroza (1999). However, based on comparison with our lower quality catalogue, quality restrictions exert a large effect on the spatial distribution of data in this region with a bias towards the more southerly 1992 Joshua Tree aftershocks. It is likely that these restrictions also have an effect on the observed dominant faulting style, and we therefore choose not to place strong emphasis on the result of dominant normal faulting in this region. Nevertheless, the existence of mechanisms in both \hat{E}_{ij}^B and \hat{E}_{ij}^E

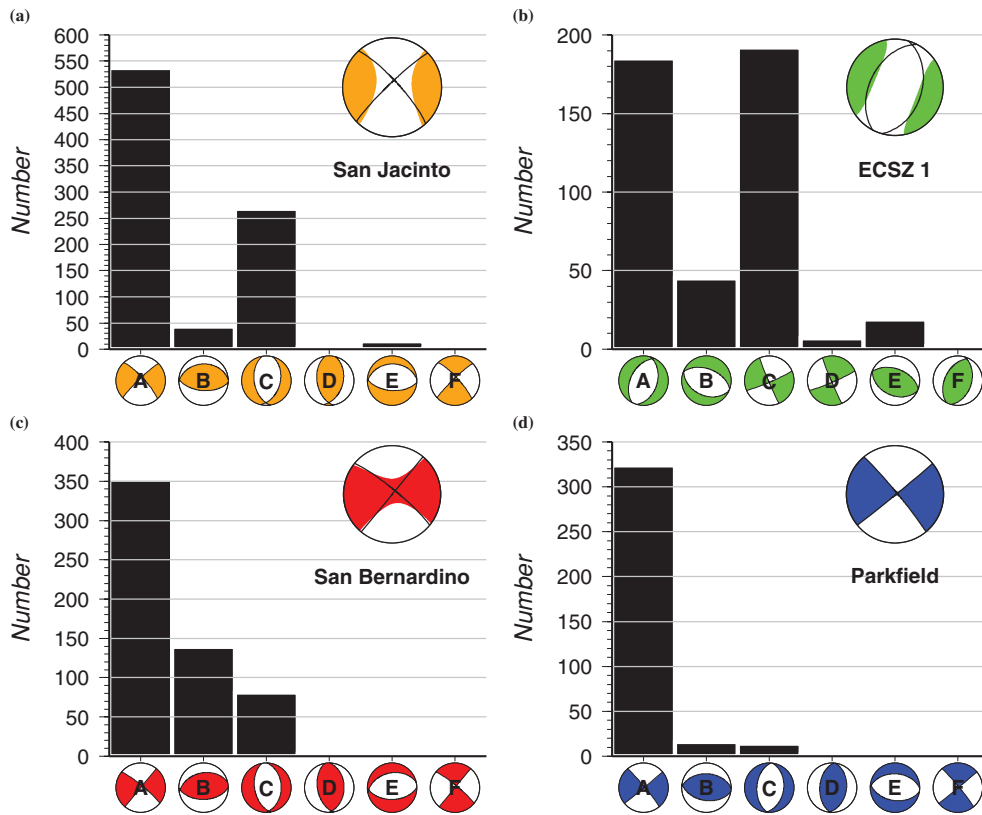


Figure 5. Partitioning of focal mechanism styles based on Eq. 6 for (a) San Jacinto Fault, (b) ECSZ 1 (c) SAF - San Bernardino and (d) SAF - Parkfield section. Large beachballs in the top right of the plots show the \hat{E}_{ij} result for each fault zone. Smaller beachballs beneath the horizontal axes show the DC orientations corresponding to each of the six categories in Eq. 6 which depend on \hat{E}_{ij}^{DC} for each zone.

categories, where compressive and extensive axes oppose each other, indicate a fairly heterogeneous stress field for the fault zone (*cf.* Hardebeck & Hauksson 2001).

4.5 San Jacinto partitioning

Figs 6 and 7 illustrate the spatial partitioning of the San Jacinto fault zone focal mechanisms into \hat{E}_{ij}^A , \hat{E}_{ij}^B and \hat{E}_{ij}^C . We disregard \hat{E}_{ij}^D , \hat{E}_{ij}^E and \hat{E}_{ij}^F due to the negligible number of data in these categories. This spatial partitioning is shown by comparing the relative density of epicentres (Fig. 6) and of hypocentre locations on strike-depth projections (Fig. 7) for focal mechanisms belonging to each faulting style category. We display results for the sub-populations in terms of percentage, computed by dividing the sub-population density by the overall density. For display purposes we neglect areas where the overall density is less than 0.2 km^{-2} in Fig. 6 and less than 0.3 km^{-2} in Fig. 7 when calculating the percentages.

The density maps highlight that most of the seismicity is confined to a few clusters, and we label these with the letters U, V, W, X, Y, Z. The largest of these clusters, V, corresponds to the location of a $M_L = 5.1$ earthquake in October, 2001, though roughly 40 per cent of the earthquakes at this location occurred before that event. We find that consistent with the summed tensor result, strike-slip faulting accounts for half or more of the seismicity in all of the clusters except for parts of Y and Z. This illustrates a regional dominance of strike-slip faulting. The negative value of r_{CLVD} for the region (Fig. 3) indicates a dominance of normal faulting over reverse faulting mechanisms for the region, as confirmed in Fig. 5.

However, Figs 6 and 7 demonstrate that this normal faulting is not distributed uniformly throughout the seismicity, but is concentrated in the clusters V, Y and Z, implying that the distribution of seismicity with respect to the geometry of local structures exert significant influence on the fault zone heterogeneity. If we define a cluster to be approximately homogeneous when over 75 per cent of the seismicity is of one type, then U, X and the centre of Y may be regarded as homogeneous. However, there seems to be some degree of heterogeneity in all clusters, at the edge or throughout, making it difficult to generalize. At the scale of the clusters we do not find a strong quantifiable correlation between heterogeneity of the focal mechanisms and complexity in the surface traces.

Fig. 8 presents analogous partitioning results for the fault zone focal mechanisms as a function of time and magnitude. Here, we divide the population into bins of (a) 1 yr and (b) $0.25M_L$ units, and then compute the percentage of mechanisms in those bins that are of type \hat{E}_{ij}^A (strike-slip faulting), \hat{E}_{ij}^B (reverse faulting) and \hat{E}_{ij}^C (normal faulting).

As shown by the cumulative number of focal mechanisms in Fig. 8a, the rate is roughly constant at ~ 30 per year until the jump caused by the 2001 earthquake which quickly recovers to a roughly constant higher rate of ~ 90 per year. Although we find variation in the partitioning over time, there is no indication that these changes relate to the $M_L 5.1$ earthquake or subsequent change in rate, and most of the changes can be related to the varying influence of spatial clusters in Figs 6 and 7. Cluster Y, where we observe a mixing of strike-slip and normal faulting is most active during the 1990's. The largest cluster of seismicity, V, which mixes all three faulting types and is in the middle of the fault, is active throughout the entire time

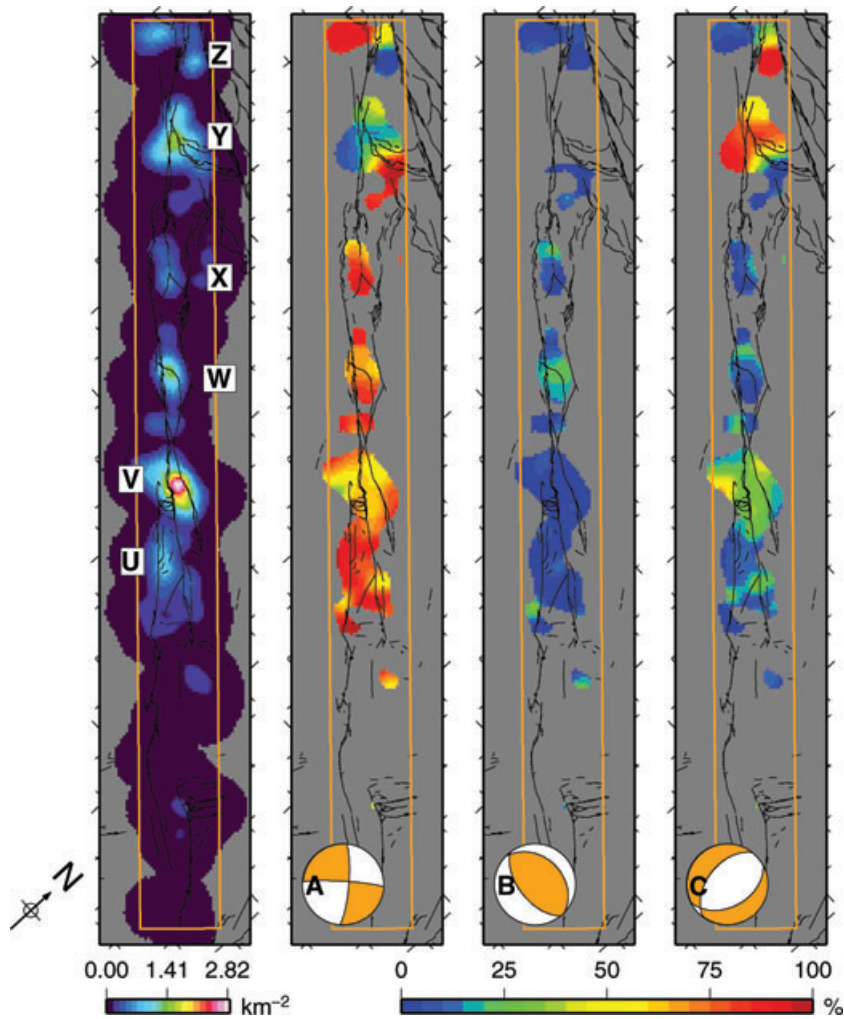


Figure 6. Smoothed density (number per km^2) of epicentre locations in the San Jacinto fault zone (see Fig. 1) compared to the percentage of that density contributed by the three DC categories \hat{E}_{ij}^A (strike-slip faulting), \hat{E}_{ij}^B (reverse faulting) and \hat{E}_{ij}^C (normal faulting). The beachballs in the bottom left of the maps, which are rotated along with the map projection, indicate the category. Smoothing of the density is performed using 2-D Gaussian kernels with standard deviation of 1 km, and percentages are only computed for points where density is greater than 0.2.

period with an increase in rate that accounts for the changes after 2001.

Fig. 8(b) shows that earthquakes in the three faulting styles approximately follow a Gutenberg-Richter distribution of magnitudes with similar b -values of ~ 1 . The increased percentage of normal and reverse faults below $M_L = 2.4$ can be explained by different magnitudes of completeness for the faulting types, indicated by the position of the lower magnitude roll-off in the power-law statistics. The distribution shapes indicate that given the relative locations of earthquakes and seismic stations, it is easier to constrain the nodal planes for the mechanisms of dip-slip than strike-slip faults when there are a small number of recordings. The faulting style with the lowest magnitude roll-off is different for other fault zones that we do not show here, suggesting that this feature is more a function of the local seismic network than of the *HASH* algorithm. Although this indicates that the network effects may cause Δr_{NORM} and $|r_{CLVD}|$ to be larger than they should be, the results given in Fig. 3 are within the bootstrap errors when we recompute E_{ij} using only $M_L \geq 2.4$ earthquakes. At the other end of the scale, an increased proportion of strike-slip faulting mechanisms for the larger magnitude bins would be consistent with a model where there is a physical limit to the size of dip-slip earthquakes, given that there are no large through-going

dipping faults in the zone. However, the differences shown here are based on a small number of data and can be reasonably explained by different a -values for the three faulting types. We therefore find little evidence for magnitude-related effects controlling the heterogeneity of the fault zone focal mechanism populations.

5 DISCUSSION

5.1 Fault zone differences

The existence of relative differences in focal mechanism heterogeneity for different fault zones, which are spatially defined by independent data, implies that there are characteristics unique to a given fault zone. As discussed below, this is likely related to a general evolution of fault zones towards smoother structures. Since there are observable differences between faults, there are limits to the use of scale-invariance to describe fault networks, as done by, for example King (1983), Turcotte (1997), Kagan (1990), which treat all faults as essentially the same. A system for which the range of length scales can be quantified is distinct from systems described as scale-invariant where there is similarity at all scales and effectively

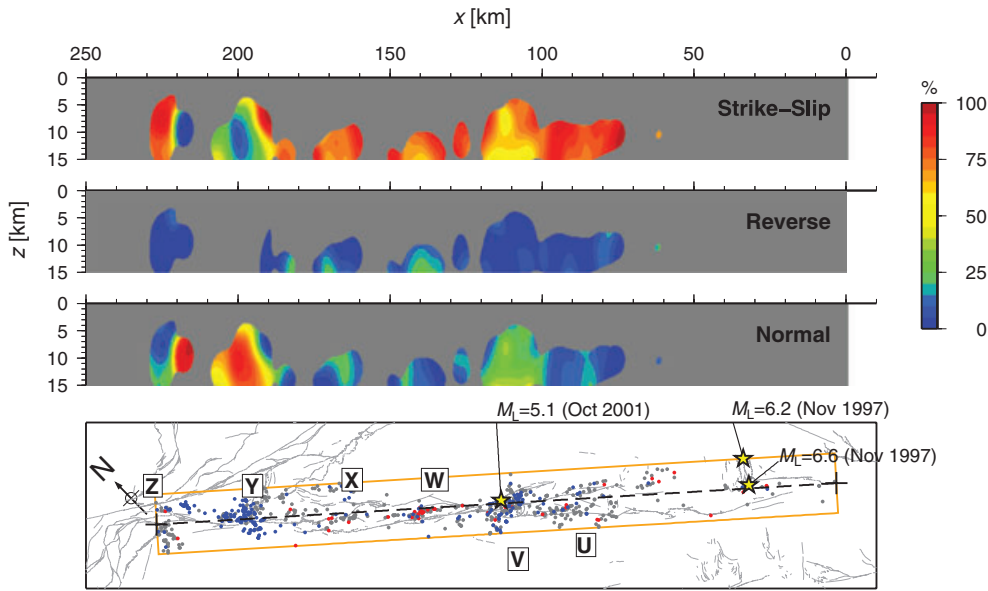


Figure 7. Percentage of the smoothed density of hypocentres projected onto a vertical fault plane aligned with the San Jacinto fault zone for the three DC categories \hat{E}_{ij}^A (strike-slip faulting), \hat{E}_{ij}^B (reverse faulting) and \hat{E}_{ij}^C (normal faulting). The profiles have a vertical exaggeration factor of 2, and the along strike distance is computed by projecting onto the dashed line shown in the lower map. Black, red and blue dots represent, respectively, the epicentres of the strike-slip, reverse and normal faulting earthquakes on that map. Yellow stars in the lower plots indicate the hypocentres of the three $M_L > 5$ earthquakes that occurred in the zone during the time period, with magnitude and year noted next to each.

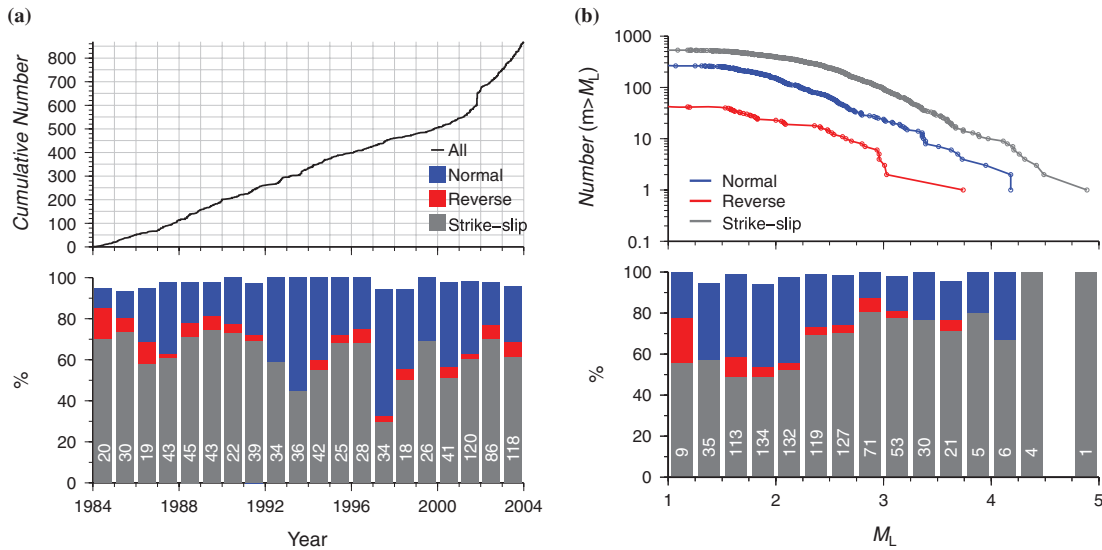


Figure 8. (a) Time versus number of earthquakes in the San Jacinto fault zone for each of the three categories \hat{E}_{ij}^A (strike-slip faulting, grey), \hat{E}_{ij}^B (normal faulting, blue) and \hat{E}_{ij}^C (reverse faulting, red). The upper plot shows the cumulative number of focal mechanisms as a function of time. The lower plot shows boxes indicating the percentage of mechanisms within 1 yr bins corresponding to the three main faulting styles. The total number of mechanisms in each bin is given by numbers within the boxes. The boxes often sum to less than 100 per cent because we omit mechanisms of types \hat{E}_{ij}^C , \hat{E}_{ij}^D and \hat{E}_{ij}^E (b) Magnitude versus number of earthquakes for each of the three faulting categories. The upper plot shows frequency-size distributions of focal mechanisms in the categories. The lower plot shows the percentage of mechanisms within $0.25 M_L$ unit bins corresponding to the three main faulting styles, with the total number of mechanisms for each bin noted by numbers inside the boxes.

no length scales of importance. Bailey *et al.* (2009) showed that the earthquake deformation patterns in southern California are not truly scale-invariant, and here we show that departures from scale invariance can be related to the heterogeneity of specific fault zones. Ben-Zion (2008) provides a detailed discussion of this general issue in relation to dynamics of earthquakes and faults.

The usefulness of the CLVD component of E_{ij} in quantifying differences between fault zone populations of DC mechanisms indicates the importance of measuring asymmetry in the mechanism orientation distributions. Previous studies that quantify heterogeneity of a set of focal mechanism orientations use the distribution of minimum rotation angles between all pairs of DC orientations

(e.g. Kagan 1990; Hardebeck 2006), or the distribution of the vertical components of the three eigenvectors (Frohlich 1992). Although these methods give a more complete description of focal mechanism heterogeneity than our two measures, they cannot always constrain the asymmetry that would lead to a CLVD component. This study highlights the advantage of pursuing several approaches simultaneously to understand focal mechanism heterogeneity.

5.2 Relationships between fault trace and focal mechanism properties

We find two correlations between the characteristics of focal mechanism orientation heterogeneity and properties of the fault geometry as mapped at the surface. This indicates that surface properties of a fault zone correspond to heterogeneity at depth. In other words, the geometry of the fault zone resulting from 10^4 – 10^6 yr timescales of strain exerts a control on ~ 20 yr of small earthquakes.

Ben-Zion & Sammis (2003) summarized evidence for an evolution of faults over geologic timescales towards smoother geometries with a narrower range of size scales. The correlation between τ_1/τ_2 and Δr_{NORM} shows that the differences in smoothness and hence the results of such evolution are detectable in the earthquake record. Characteristics of fault traces have previously been related to the maturity of fault zones as quantified by their cumulative displacement (e.g. Stirling *et al.* 1996). Our two measures of fault complexity (based on focal mechanisms and fault traces) show a generally negative correlation to different estimates of cumulative displacement (Bailey 2009), though the correlations are not strong and difficult to quantify given the nature of uncertainty in displacement estimates. In general, this suggests that evolution to smoother geometries is not a simple function of cumulative slip within a fault zone, but is likely to be influenced by other factors such as the overall orientation of the fault zone (as indicated by the focal mechanism results here) and slip rate (e.g. Wechsler *et al.* 2010).

The relation between the dominant fault azimuth and asymmetry in the distribution of focal mechanism orientations may be explained by considering the direction of the fault relative to the plate loading. As illustrated in Fig. 9(a), slip on faults parallel to the direction of relative plate motion can efficiently release the elastic strain energy built up by plate loading. However, slip on a fault that is misaligned will lead to a deficiency in extension if the plate motion pulls away from the fault (Fig. 9b), or compression if the plate motion pushes into the fault (Fig. 9c). As indicated by the figures, these deficiencies can be released by reverse or normal faults with the appropriate orientations.

This explanation implies a difference between the strain release in the large earthquakes which rupture along the entire or most of the fault zone, and in the population of small earthquakes when the main fault is effectively locked. Geodetic and geologic data show that large through-going faults take the dominant role in releasing elastic strains built up by the ongoing relative plate motions. The results here indicate that when those large faults are locked, the low magnitude seismicity responds to the ongoing plate motion as well as the inability of the large faults to fully release those strains. This is observable in both the fault zones where there has been a moderate to large earthquake during the time period of this study (Parkfield, ECSZ 1 and ECSZ 2), as well as other fault zones where there has not been a large earthquake for over a hundred years. The existence of dominant fault surfaces with orientations that are not aligned with the local plate motion indicates an inefficiency in the manner that the strain energy is released over a plate boundary. This is consistent with the evolution of fault zones towards smoother structures, since non-optimally aligned faults that are smooth can become focuses of strain energy release due to the ease of rupture propagation, despite the existence of more optimally aligned (but rougher) faults in the same zone.

The obtained correlations between surface trace properties and the focal mechanism heterogeneity measures are reasonable, though it is difficult to explain all of the results since the fault zones that correlate least well are different for the two factors investigated. For τ_1/τ_2 versus Δr_{NORM} , the correlation is not as strong partly because of a steeper trend for two of the fault zones sampled by fewer focal mechanisms (ECSZ 2 and Coachella). This may relate to the strong trade off between the number and quality of data discussed in Appendix B, particularly since these two regions lie towards the edge of the southern California seismic network. The relations might be better resolved given greater numbers of high quality data. For α_u versus r_{CLVD} , the San Jacinto Fault and Coachella Section of the SAF show the strongest divergence from the trend. These fault zones are the most southeasterly of the data sets and may indicate that our explanation (Fig. 9) is not completely suitable close to the termination of the San Andreas Fault System. The loading stress may be modified in the southern regions due to the transition to the triple junction to the south, such that there is more extension and an increased number of normal faulting mechanisms to the east of the main plate boundary (Platt *et al.* 2008), overlaying the fault based effect.

Models for plate motion based on GPS data for the entire southern California region indicate slightly more westerly azimuths for the relative plate directions than those based on transform faults and magnetic lineations (Table 1 of Meade & Hager 2005). This

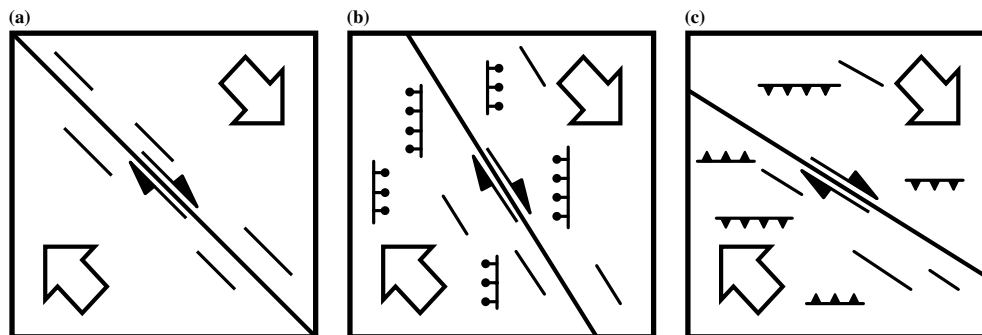


Figure 9. Schematic illustrations showing how (a) faults parallel to plate motion lead to homogeneous faulting (b) plate motion that pulls away from the fault leads to second-order normal faulting and (c) plate motion that pushes into the fault leads to second-order reverse faulting.

may partially explain the separation of positive and negative values of r_{CLVD} at an azimuth west of the relative plate motion azimuth (Fig. 4a), though there are no estimates as great as -45° .

5.3 Fault style partitioning

In Section 4.4 we show that the focal mechanism populations can be partitioned into, at most, four different faulting styles. The absence of many mechanisms with \hat{E}_{ij}^C , \hat{E}_{ij}^D and \hat{E}_{ij}^E orientations indicates that the mechanisms are not as diverse as found in some studies (e.g. Zoback *et al.* 1993; Rivera & Kanamori 2002), which is likely to be due to the restriction to higher quality focal mechanisms (Hardebeck 2006). Since mechanisms of \hat{E}_{ij}^A , \hat{E}_{ij}^B and \hat{E}_{ij}^C can be generated by different fault orientations responding to the same loading tensor, relatively smooth variations in the stress field would be adequate to explain our results (*cf.* Hardebeck 2006). However, variations of both the P and T axes orientations over a 90° range, the presence of at least three faulting styles, as well as clear asymmetry implies that the distribution of fault orientations in a fault zone is often quite complex, and cannot be described by minor symmetric variations about a mean.

The results presented in Section 4.5 show that spatial factors of the seismicity exert a stronger control on the focal mechanism heterogeneity than temporal or magnitude based factors. This indicates the importance of existing fault structures over mainshock–aftershock interactions. The observation of distinct localized clusters in Figs 6 and 7 also serve as a caveat to the interpretation of the focal mechanism data as representing heterogeneity over the entire examined fault zones. These clusters exist in what would be termed aftershock sequences as well as background seismicity. Under typical assumptions of linear elasticity and linear elastic fracture mechanics, concentrations of stress occur at geometrical heterogeneities (e.g. Broberg 1999), and it is likely that similar concentrations of stress around faults lead to clusters of seismicity in nature. The employed focal mechanism data would therefore represent a bias towards the heterogeneous parts of the fault zones. If there are ‘locked’ parts of the fault zone, which only fail in large ($M_L \geq 6$) earthquakes, it is possible that much of the strain release would not be as heterogeneous as in these clusters of low magnitude seismicity. This is consistent with the observation that all of the largest earthquakes are of strike-slip type (Section 4.5), though we find little evidence that more homogeneous clusters are associated with smoother parts of the San Jacinto Fault zone. Despite these considerations, the relative differences in heterogeneity levels are still applicable to the entire fault zones, as implied by the correlations with α_u and τ_1/τ_2 . Due to the relative lack of seismicity on the smooth sections of the San Andreas Fault, we consider it likely that a more complete sample of the fault zones which is not limited to clusters would make the differences in heterogeneity more apparent.

The results in Section 4.5 also highlight the effect of network sampling on our results. Both temporal and spatial variations in the sampling of earthquakes can lead to biases towards different focal mechanism styles when imposing quality restrictions on the focal mechanism catalogue. As such we are not only limited in the spatial sampling of the fault zone, but even in the sampling of the earthquakes that occurred. However, results in Appendix B show that differences between fault zones are apparent regardless of the data quality. Although it is difficult to constrain the biases towards spatial sampling and particular focal mechanism types, it

is unlikely that these biases can explain the observed differences between fault zones.

6 CONCLUSIONS

Source mechanism summations are useful in quantifying variation in populations of focal mechanisms. Our results indicate that long-term properties of fault zones represented by their fault traces correlate with focal mechanism heterogeneity that differs between fault zones. The scatter in focal mechanism orientations shows a reduction of complexity consistent with fault trace geometry that we relate to the evolutionary maturity of the fault zone. The asymmetry in the focal mechanism orientations, related to the fault zone azimuth, leads to a component of heterogeneity that is controlled by the overall orientation of the fault zone with respect to local plate motion. We find that the spatial clusters of seismicity strongly affect the distribution of focal mechanism orientation. The use of focal mechanism data of the type done here and other studies is therefore limited by how representative spatial clusters are in terms of the entire fault zone.

ACKNOWLEDGMENTS

We thank Jeanne Hardebeck for generating the *HASH* catalogue of focal mechanisms used in this work, James Dolan and Mike Oskin for answering specific questions about southern California faults, and Susan Rhea for answering our queries about the USGS fault database. This research was supported by the National Science Foundation (grant EAR-0908903) and Southern California Earthquake Center (based on NSF Cooperative Agreement EAR-0106924 and USGS Cooperative Agreement 02HQAG0008). The manuscript benefited greatly from useful comments given by three anonymous reviewers and the editor Massimo Cocco. Nearly all figures were generated using GMT (Wessel & Smith 1998).

REFERENCES

- Amelung, F. & King, G., 1997. Large-scale tectonic deformation inferred from small earthquakes, *Nature*, **386**, 702–705.
- Ando, R., Shaw, B.E. & Scholz, C.H., 2009. Quantifying natural fault geometry: statistics of splay fault angles, *Bull. seism. Soc. Am.*, **99**(1), 389–395.
- Bailey, I.W., 2009. Heterogeneity of earthquake stress drops, focal mechanisms and active fault zones, *PhD thesis*. University of Southern California, Los Angeles, CA.
- Bailey, I.W. & Ben-Zion, Y., 2009. Statistics of earthquake stress drops on a heterogeneous fault in an elastic half-space, *Bull. seism. Soc. Am.*, **99**(3), 1786–1800, 10.1785/0120080254.
- Bailey, I.W., Becker, T.W. & Ben-Zion, Y., 2009. Patterns of coseismic strain computed from southern California focal mechanisms, *Geophys. J. Int.*, **177**, 1015–1036, doi:10.1111/j.1365-246X.2009.04090.x.
- Ben-Zion, Y., 2008. Collective behavior of earthquakes and faults: continuum-discrete transitions, progressive evolutionary changes and different dynamic regimes, *Rev. Geophys.*, **46**, RG4006, doi:10.1029/2008rg000260.
- Ben-Zion, Y. & Rice, J.R., 1995. Slip patterns and earthquake populations along different classes of faults in elastic solids, *J. geophys. Res.*, **100**, 12959–12983.
- Ben-Zion, Y. & Sammis, C.G., 2003. Characterization of fault zones, *Pure appl. Geophys.*, **160**, 677–715.
- Ben-Zion, Y., Eneva, M. & Liu, Y., 2003. Large earthquake cycles and intermittent criticality on heterogeneous faults due to evolving stress and seismicity, *J. geophys. Res.*, **108**(B6), 2307–2328, doi:10.1029/2002JB002121.

- Broberg, K.B., 1999. *Cracks and Fracture*, Academic Press, San Diego, California.
- California Geological Survey & U.S. Geological Survey, 2010. Quaternary fault and fold database for the United States, Available at: <http://earthquake.usgs.gov/regional/qfaults/> (accessed 2010 January).
- DeMets, C., Gordon, R.G., Argus, D.F. & Stein, S., 1994. Effect of recent revisions to the geomagnetic reversal time scale on estimates of current plate motions, *Geophys. Res. Lett.*, **21**(20), 2191–2194.
- Dieterich, J.H. & Smith, D.E., 2009. Non-planar faults: mechanics of slip and off-fault damage, *Pure appl. Geophys.*, **166**(10–11), 1799–1815, doi:10.1007/s00024-009-0517-y.
- Felzer, K.R. & Beroza, G.C., 1999. Deep structure of a fault discontinuity, *Geophys. Res. Lett.*, **26**(14), 2121–2124.
- Fischer, K.M. & Jordan, T.H., 1991. Seismic strain rate and deep slab deformation in Tonga, *J. geophys. Res.*, **96**, 14 429–14 444.
- Fisher, N.I., 1993. *Statistical Analysis of Circular Data*, Vol. 1, Cambridge University Press, New York.
- Frohlich, C., 1992. Triangle diagrams: ternary graphs to display similarity and diversity of earthquake focal mechanisms, *Phys. Earth planet. Inter.*, **75**(1–3), 193–198.
- Frohlich, C. & Apperson, K.D., 1992. Earthquake focal mechanisms, moment tensors, and the consistency of seismic activity near plate boundaries, *Tectonics*, **11**(2), 279–296.
- Hardebeck, J.L., 2006. Homogeneity of small-scale earthquake faulting, stress, and fault strength, *Bull. seism. Soc. Am.*, **96**(5), 1675–1688.
- Hardebeck, J.L. & Hauksson, E., 2001. Crustal stress field in southern California and its implications for fault mechanics, *J. geophys. Res.*, **106**(B10), 21 859–21 882.
- Hardebeck, J.L. & Shearer, P.M., 2002. A new method for determining first-motion focal mechanisms, *Bull. seism. Soc. Am.*, **92**, 2264–2276.
- Hardebeck, J.L., Shearer, P.M. & Hauksson, E., 2005. A new earthquake focal mechanism catalog for southern California, in *2005 SCEC Annual Meeting Abstracts*, p. 130, Southern California Earthquake Center. <http://www.data.scec.org/research/altcatalogs.html> (accessed 2008 July).
- Hillers, G., Ben-Zion, Y. & Mai, P.M., 2006. Seismicity on a fault controlled by rate- and state-dependent friction with spatial variations of the critical slip distance, *J. geophys. Res.*, **111**(B01403), doi:10.1029/2005JB003859.
- Hillers, G., Mai, P.M., Ben-Zion, Y. & Ampuero, J.-P., 2007. Statistical properties of seismicity of fault zones at different evolutionary stages, *Geophys. J. Int.*, **169**(19), 515–533, doi:10.1111/j.1365-246X.2006.03275.x.
- Julian, B.R., Miller, A.D. & Foulger, G.R., 1998. Non-double-couple earthquakes I. Theory, *Rev. Geophys.*, **36**, 525–550, doi:10.1029/98RG00716.
- Kagan, Y.Y., 1990. Random stress and earthquake statistics: spatial dependence, *Geophys. J. Int.*, **102**, 573–583.
- Kagan, Y.Y., 1991. 3-D rotation of double-couple earthquake sources, *Geophys. J. Int.*, **106**, 709–716.
- Kagan, Y.Y., 2005. Double-couple earthquake focal mechanism: random rotation and display, *Geophys. J. Int.*, **163**, 1065–1072, doi:10.1111/j.1365-246X.2005.02781.x.
- Kagan, Y.Y., 2009. On geometric complexity of earthquake focal zone and fault system: A statistical study, *Phys. Earth planet. Inter.*, **173**, 254–268, doi:10.1016/j.pepi.2009.01.006.
- Kilb, D. & Hardebeck, J.L., 2006. Fault parameter constraints using relocated earthquakes: a validation of first-motion focal-mechanism data, *Bull. seism. Soc. Am.*, **96**, 1140–1158.
- King, G.C.P., 1983. The accommodation of large strains in the upper lithosphere of the earth and other solids by self-similar fault systems: the geometrical origin of *b*-value, *Pure appl. Geophys.*, **121**(5), 761–815.
- King, G.C.P. & Nábělek, J., 1985. The role of bends in faults in the initiation and termination of earthquake rupture, *Science*, **228**, 984–987.
- Knopoff, L. & Randall, M.J., 1970. The compensated linear vector dipole: a possible mechanism for deep earthquakes, *J. geophys. Res.*, **75**, 4957–4963.
- Kostrov, B.V., 1974. Seismic moment and energy of earthquakes and seismic flow of rock, *Phys. Solid Earth*, **1**, 23–40.
- Lin, G., Shearer, P.M. & Hauksson, E., 2007. Applying a three-dimensional velocity model, waveform cross correlation, and cluster analysis to locate southern California seismicity from 1981 to 2005, *J. geophys. Res.*, **112**(B12309), doi:10.1029/2007JB004986.
- Mardia, K.V. & Jupp, P.E., 1999. *Directional Statistics*, 2nd edn, John Wiley and Sons, Chichester.
- McKenzie, D.P., 1969. The relation between fault plane solutions for earthquakes and the directions of the principal stresses, *Bull. seism. Soc. Am.*, **59**(2), 591–601.
- Meade, B.J. & Hager, B.H., 2005. Block models of crustal motion in southern California constrained by GPS measurements, *J. geophys. Res.*, **110**, doi:10.1029/2004JB003209.
- Michael, A.J., 1987. Use of focal mechanisms to determine stress; a control study, *J. geophys. Res.*, **92**, 357–368.
- Platt, J.P., Kaus, B. & Becker, T.W., 2008. The mechanics of continental transforms: an alternative approach with applications to the San Andreas system and the tectonics of California, *Earth planet. Sci. Lett.*, **274**(3–4), 380–391.
- Press, W.H., Teukolsky, S.A., Vetterling, W.H. & Flannery, B.P., 1992. *Numerical Recipes in C*, 2nd edn, Cambridge University Press, New York.
- Rivera, L. & Kanamori, H., 2002. Spatial heterogeneity of tectonic stress and friction in the crust, *Geophys. Res. Lett.*, **29**, doi:10.1029/2001GL013803.
- Rockwell, T.K. & Ben-Zion, Y., 2007. High localization of primary slip zones in large earthquakes from paleoseismic trenches: observations and implications for earthquake physics, *J. geophys. Res.*, **112**(B10304), doi:10.1029/2006JB004764.
- Sipkin, S.A. & Silver, P.G., 2003. Characterization of the time-dependent strain field at seismogenic depths using first-motion focal mechanisms: observations of large-scale decadal variations in stress along the San Andreas Fault system, *J. geophys. Res.*, **108**(B7), 2339, doi:10.1029/2002JB002064.
- Stirling, M.W., Wesnousky, S.G. & Shimazaki, K., 1996. Fault trace complexity, cumulative slip, and the shape of the magnitude-frequency distribution for strike-slip faults: a global survey, *Geophys. J. Int.*, **124**(3), 833–868, doi:10.1111/j.1365-246X.1996.tb05641.x.
- Thurber, C., Zhang, H., Waldhauser, F., Hardebeck, J.L., Michael, A. & Eberhart-Phillips, D., 2006. Three-dimensional compressional wavespeed model, earthquake relocations, and focal mechanisms for the Parkfield, California, region, *Bull. seism. Soc. Am.*, **96**(4B), S38–S49, doi:10.1785/0120050825.
- Turcotte, D.L., 1997. *Fractals and Chaos in Geology and Geophysics*, 2nd edn, Cambridge University Press, Cambridge, England/New York.
- Wechsler, N., Ben-Zion, Y. & Christofferson, S., 2010. Evolving geometrical heterogeneities of fault trace data, *Geophys. J. Int.*, **182**, 551–567, doi:10.1111/j.1365-246X.2010.04645.x.
- Wesnousky, S.G., 1988. Seismological and structural evolution of strike-slip faults, *Nature*, **335**, 340–343, doi:10.1038/335340a0.
- Wesnousky, S.G., 2006. Predicting the endpoints of earthquake ruptures, *Nature*, **444**, 358–360.
- Wessel, P. & Smith, W.H.F., 1998. New, improved version of the Generic Mapping Tools released, *EOS, Trans. Am. geophys. Un.*, **79**(47), 579.
- Zoback, M.D. et al., 1993. Upper-crustal strength inferred from stress measurements to 6 km depth in the KTB borehole, *Nature*, **365**, 633–635, doi:10.1038/365633a0.
- Zöller, G., Holschneider, M. & Ben-Zion, Y., 2005. The role of heterogeneities as a tuning parameter of earthquake dynamics, *Pure appl. Geophys.*, **162**(6–7), 1027–1049.

APPENDIX A: FAULT ZONE SELECTION

Table A1 shows the number of focal mechanisms and specifies the end points of the great circle arcs used to define each of the fault zones. We consider all faults from the quaternary fault database (California Geological Survey & U.S. Geological Survey 2010) as active and extract fault segments based on the distance of vertices from the great circle arcs that approximate our fault zones. For the Elsinore fault zone, we exclude the southern-most fault section due

Table A1. Summary of data for the fault zones and definitions of fault zones used in this study. $N(\text{High})$ refers to the number of A and B quality focal mechanisms, and $N(\text{Lower})$ refers to the number with $FPU < 45^\circ$. Combined fault length refers to the cumulative length of all fault segments included in the fault zone. The coordinates for the end points of the great circle arcs are given in degrees latitude and longitude.

Name	$N(\text{High})$	$N(\text{Lower})$	Combined Length of Fault Segments (km)	Great Circle End Points
San Jacinto	869	6,669	1,156.0	[32.83N, 115.61W] – [34.19N, 117.45W]
Elsinore	78	1,336	639.3	[32.58N, 115.78W] – [33.99N, 117.82W]
Garlock	46	693	467.3	[34.83N, 118.85W] – [35.50N, 117.45W]
ECSZ 1	450	8,710	590.4	[33.92N, 116.30W] – [34.67N, 116.63W]
ECSZ 2	50	1,772	378.1	[34.25N, 116.10W] – [34.87N, 116.48W]
SAF - Coachella	28	313	310.6	[33.35N, 115.73W] – [33.78N, 116.25W]
SAF - Bernardino	584	4,097	880.5	[33.78N, 116.25W] – [34.27N, 117.45W]
SAF - Mojave	82	1,148	684.1	[34.27N, 117.45W] – [34.73N, 118.60W]
SAF - Parkfield	358	3,666	347.8	[35.67N, 120.22W] – [36.32N, 120.90W]

to lack of seismic data. For the Garlock Fault, the eastern section is removed from the analysis since the change in fault strike is not sampled by the focal mechanism data. For the Parkfield section of the San Andreas Fault, the longitude and latitude limits are the extent of the catalogue data.

APPENDIX B: TRADE-OFF BETWEEN NUMBER AND QUALITY OF FOCAL MECHANISMS

Most earthquakes are small and not recorded by many seismic stations. Fewer recordings of a given event make it more difficult to constrain the focal mechanism orientation. Hence there is a trade off between the number of earthquakes and the quality level of a data set. The advantages of using a higher number of data are that statistics are less affected by outliers, and that more of the fault zone is likely to be sampled by the data. However, greater uncertainty in the focal mechanism data will lead to greater variations in the focal mechanism orientations. This is important with relation to our study since uncertainties may overshadow the physical heterogeneity sampled by the focal mechanisms. We investigate this trade off by comparing results for analysis of a low quality catalogue, where

$FPU < 45^\circ$, to those from the higher quality catalogue used in our main study with quality restrictions outlined in Section 2.2. The lower quality catalogue contains roughly ten times the number of data in the higher quality catalogue (Table A1).

In Fig. B1 we show the results for r_{CLVD} and Δr_{NORM} computed from the lower quality data, analogous to Fig. 3, as well as the differences between absolute values for low and high quality data. For three out of nine of the fault zones the decrease in quality restrictions lead to lower values of $|r_{CLVD}|$, whereas for eight fault zones there is an increase in Δr_{NORM} . The notable exceptions (the Garlock Fault and the Mojave Section of the SAF) have few data in the higher quality catalogue, although other fault zones that fit this pattern have fewer data (Table A1). The bootstrap error bounds, which constrain the robustness of r_{CLVD} and Δr_{NORM} based on the number of data, are smaller in all cases for lower quality data due to larger data sets. In both cases, there is no correlation between the size of the error bounds and values of r_{CLVD} and Δr_{NORM} . Although the decrease in data quality leads to a general reduction in the relative differences of focal mechanism heterogeneity between fault zones, particularly for the Parkfield section of the SAF, distinct differences persist between the fault sections.

One explanation for the differences in heterogeneity results for the two catalogues [Fig. B1(b)] is that there are changes in the

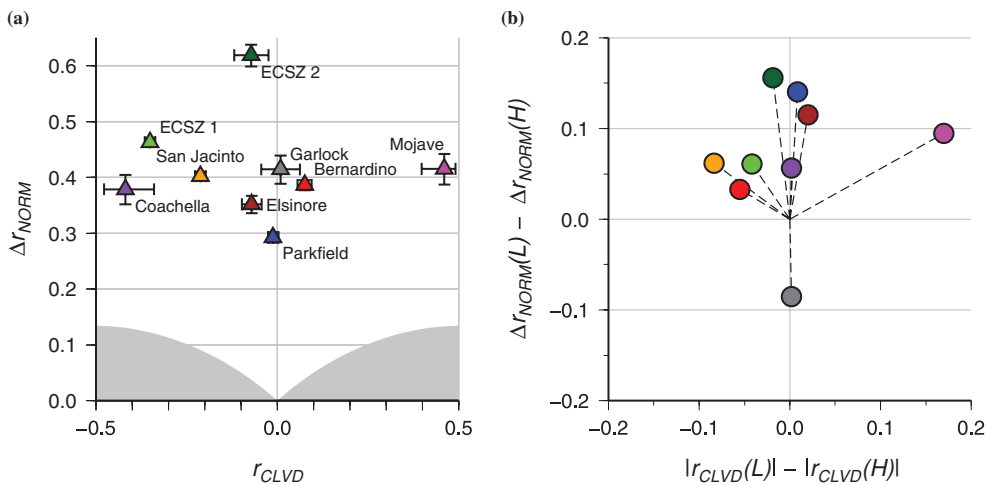


Figure B1. (a) Same as Fig. 3, but incorporating lower quality focal mechanisms such that $FPU < 45^\circ$. (b) The difference between the results in Fig. 3 and (a) presented as the difference in absolute values to highlight increasing or decreasing heterogeneity. L refers to the lower quality catalogue whereas H refers to the A and B quality data.

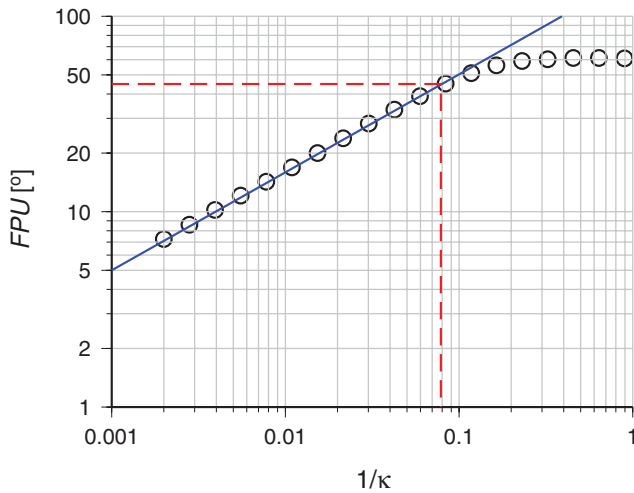


Figure B2. Values of FPU computed for populations of DCs generated by random sampling the von Mises–Fisher kernel (eq. B1) 10 000 times using different values of κ , then computing FPU using the method of Hardebeck & Shearer (2002). A linear relationship between $\log(FPU)$ and $-\log(\kappa)$ is fitted for $FPU < 45^\circ$ by least squares and overlain as a solid blue line. The red dashed line shows the cut-off of the scaling relationship.

sampling of the fault structure when including more data. We illustrate that such a signal would be overshadowed by data uncertainties using an approach based on a kernel density representation for the focal mechanisms. By representing each DC orientation as a kernel function with width related to uncertainty, then randomly sampling from the combined kernel density using N points many times, we incorporate uncertainties related to the number of data N and the data quality into the heterogeneity quantities for each fault zone.

To simulate uncertainty of a single DC orientation, we use a kernel function of the form

$$f(\Omega) = C e^{\kappa \cos(\Omega/2)}, \quad (\text{B1})$$

where Ω is the rotation angle of principle strain axes from a mean orientation, κ is a concentration parameter, and C is a normalizing factor.

Kilb & Hardebeck (2006) found that FPU is the most representative quantification of focal mechanism quality for *HASH* generated data. We relate κ to FPU by

$$\kappa = A e^{-B \ln(FPU)}, \quad (\text{B2})$$

when $FPU \leq 45^\circ$, with $A = 2.688 \times 10^4$ and $B = 2.011$, calculated from a fit to simulated data (Fig. B2). The scaling relation appears to breakdown for $FPU > 45^\circ$ and tends towards a uniform distribution ($\kappa = 0$). This indicates that there is little informational value in using focal mechanisms with $FPU > 45^\circ$.

We combine eqs (B1) and (B2) to generate a density of kernels for the low and higher quality catalogues of each fault zone. By random resampling of a given kernel density using N points, we can estimate values for Δr_{NORM} and r_{CLVD} describing heterogeneity that incorporates variable uncertainty within the data set. Repeating this resampling 10 000 times describes the robustness of our estimates given the number of data, and we display the median with 75 per cent confidence limits for the values of r_{NORM} and r_{CLVD} in Fig. B3. As well as displaying results for kernel densities of the low and higher quality data, we generate a third kernel density where the mean DC orientations of the kernels are randomly selected from

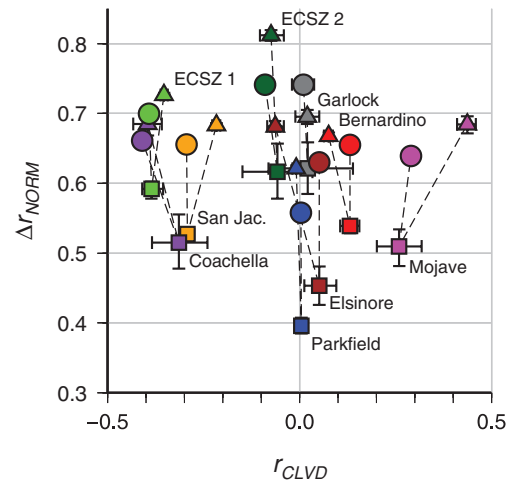


Figure B3. Angular variation of the P and T axes and values of Δr_{NORM} for a single dominant faulting type with different values of κ . (a) Red and blue circles show the orientation of 10 000 P and T axes, respectively, when $\kappa = 200$. A black dashed line circle shows θ_{90} , the angle from the mean within which 90 per cent of the simulated data are located. (b) Red and blue circles show the orientation of 10 000 P and T axes, respectively, when $\kappa = 10$. Black dashed line circle shows θ_{90} for five different values of κ . (c) The relationship between θ_{90} and Δr_{NORM} for the simulated data sets where there is no mixing of fault types.

the higher quality catalogue, but using the same number of kernels and values of FPU as the lower quality catalogue. This allows us to test how much the increased uncertainty of the low quality catalogue influences the heterogeneity measures. The differences between results for the low and higher quality catalogues are similar to those observed in Fig. B1. However, differences in Δr_{NORM} are much greater due to the increased uncertainty in lower quality data. The results for Δr_{NORM} from the case where uncertainty is added to the higher quality data are similar to values for the lower quality data. This indicates that changes in Δr_{NORM} when including lower quality data can be explained by data uncertainty, and there is little extra information about the physical heterogeneity of the fault zones.

The changes in r_{CLVD} due to the simulated effects of increased uncertainty are small, and do not explain the differences between results for the low and higher quality data. However, this is unsurprising given that our kernel function (eq. B1) does not incorporate rotational asymmetry. Hence, either the kernel function is inappropriate to model the uncertainties, or the physical heterogeneity measured by the lower quality data is different. It is likely that asymmetry exists in the uncertainty and results from limitations in the distribution of the seismic stations to sample the focal sphere of the earthquake. Furthermore, similar factors may lead us to preferentially sample certain orientations of focal mechanisms in the higher quality data because the local network can constrain them better. We see evidence for such bias in Section 4.5, where we show that dip-slip events are better sampled than strike-slip events at low magnitudes for the San Jacinto fault zone. Modelling the uncertainties due to network orientations is beyond the scope of this study. However, our main analysis concentrates on the higher quality data for the reasons that (1) quality restrictions imposed on multiple factors will allow for better comparison between data sets and (2) the analysis here shows that values of Δr_{NORM} can become dominated by uncertainty when using lower quality data.

APPENDIX C: INTERPRETATION OF HETEROGENEITY MEASURES USING NUMERICALLY SIMULATED VARIATION OF DC ORIENTATIONS

The quantities Δr_{NORM} and r_{CLVD} provide useful measures of focal mechanism heterogeneity that are easy to compute, but their physical interpretation is non-intuitive. To better understand the type and amount of variation that can lead to different values of each quantity, we simulate variation in populations of 1000 DC focal mechanisms and compute the values of Δr_{NORM} and r_{CLVD} from each simulation. We impose variation on the population in two ways: by selecting focal mechanisms from a Fisher distribution (eq. B1) with changing values for the concentration parameter κ , and by mixing different proportions of populations with different mean orientations.

A Fisher distribution as defined in eq. (B1) leads to axially symmetric and equal variation of all three strain axes about a pre-defined mean DC orientation. We arbitrarily select a strike-slip mechanism as our mean orientation and investigate four different values of κ : 10, 20, 50, 100 and 200. The synthetic data sets are generated by Monte Carlo sampling, as described in Appendix B.

Fig. C1 displays the variation of principle strain axes for different values of κ . In these cases the κ values 10, 20, 50, 100 and 200 correspond to variation such that 90 per cent of the principle strain axes are within approximately 74°, 55°, 34°, 25° and 17° of their pre-defined mean, and values of Δr_{NORM} that are 0.71, 0.46, 0.21, 0.11 and 0.06, respectively (Fig. C1c).

To simulate asymmetry in the population we divide the 1000 focal mechanisms into subsets of strike-slip, reverse and normal faulting orientations. If we denote the mean orientation for the strike-slip faults \hat{E}_{ij}^{DC} , as defined in eq. (5), the mean DC orientations of the reverse and normal faulting orientations correspond to \hat{E}_{ij}^B and \hat{E}_{ij}^C in eq. (6). In each simulation the value of κ is constant for all three subsets. We investigate cases where the number of reverse faults N_R is 0, 100, 200, 300, 400 and 500, and the number of normal faults N_N is 0, 100, 200 and 300.

For each of the 120 synthetic data sets, we compute E_{ij} and then Δr_{NORM} and r_{CLVD} . We find that Δr_{NORM} is inversely related to the value of κ as well as being inversely related to the percentage of strike-slip events (Fig. C2a). If κ and the percentage of strike-slip events are constant, Δr_{NORM} increases as the percentages of normal

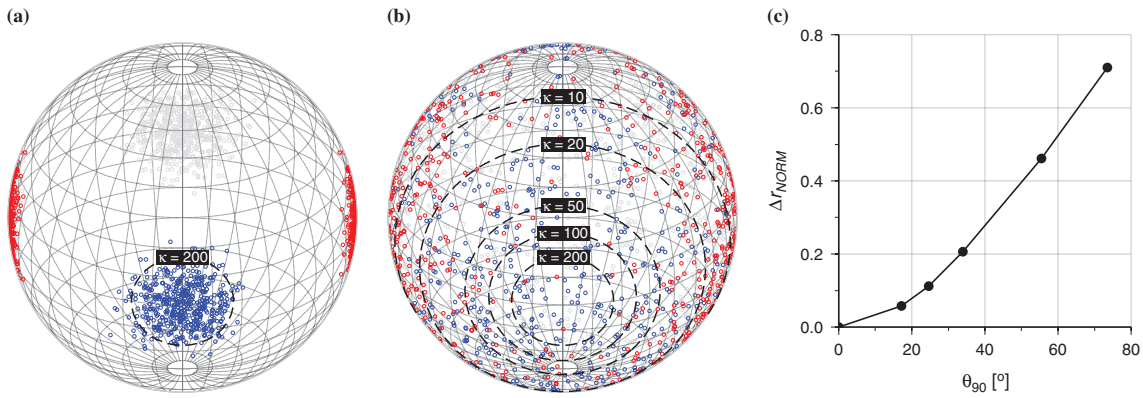


Figure C1. Compiled results for simulated DC variation based on mixing of faulting styles and Gaussian-like variations. (a) Δr_{NORM} computed from E_{ij} for each simulation as a function of the concentration parameter κ . Circle sizes represent the percentage of DC orientations from the strike-slip faulting style sub-population and colored lines show the percentage from the reverse faulting style sub-population. The remaining orientations belong to the normal faulting style sub-population. (b) r_{CLVD} computed from E_{ij} for each simulation as a function of the percentage of DC orientations from the reverse faulting style sub-population. Colors correspond to different values of κ and circle sizes correspond to the percentage of DC orientations from the normal faulting style sub-population.

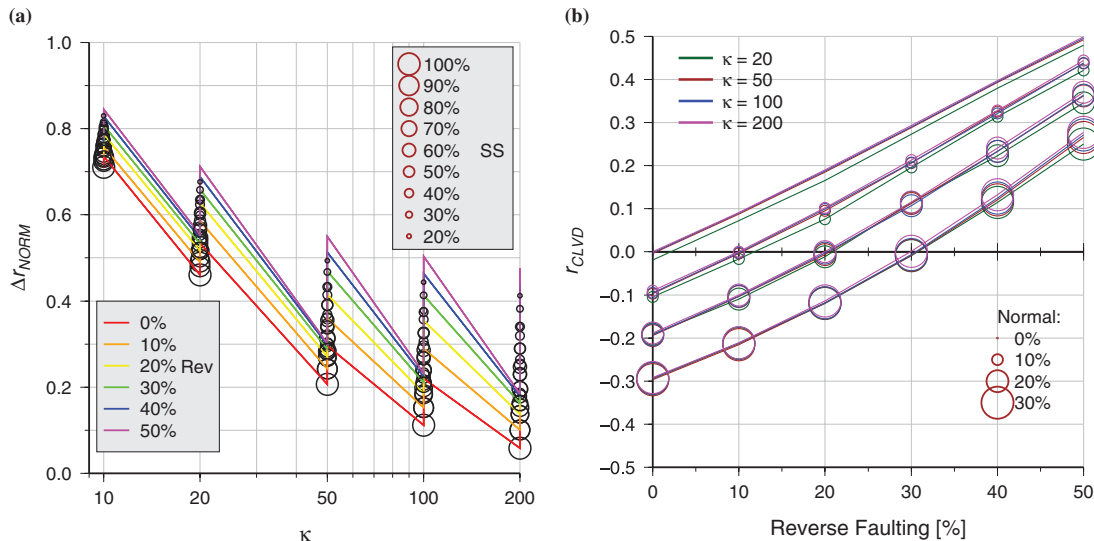


Figure C2. Average minimum rotation angle between all DC pairs in the fault zones as a function of Δr_{NORM} .

and reverse faulting mechanisms become closer together. The lowest value of Δr_{NORM} for each value of κ corresponds to cases where there is no fault mixing (Fig. C1).

Fig. C2(b) shows the positive correlation of r_{CLVD} with N_R , regardless of κ , such that r_{CLVD} is roughly equal to $(N_R - N_N)/N_{TOTAL}$. This may be stated more generally as $r_{CLVD} \approx (N_B - N_C)/(N_A + N_B + N_C)$, where $N_A \geq |N_B - N_C|$ and is the number of DCs with the first-order faulting orientation, and N_B and N_C correspond to the number in the second and third-order faulting populations. However, this relationship breaks down for lower values of κ since the mechanisms become so scattered that E_{ij} is no longer aligned with the mean strike-slip orientation. We therefore do not plot the result for $\kappa = 10$ in Fig. C2.

The cases presented here relate to variation of the entire focal mechanism, such that we are effectively simulating variation of the fault orientation and slip vector simultaneously. Alternative cases can be considered where the deviatoric loading stress orientation is kept constant, and DC orientations are computed due to maximum shear stress resolved onto fault planes of varying orientations, consistent with the assumptions made for stress inversion (Michael 1987). In the results of simulations for these cases, which are not presented here, Δr_{NORM} is related to the variation in fault plane orientations. A non-zero CLVD component can be generated in two ways: either by two separate populations of fault orientations, such that resolved shear stress leads to slip in perpendicular directions, or by introducing a CLVD component to the loading tensor. In the first case, reduction in the variation of fault orientations restricts the directions of slip possible, and the value of r_{CLVD} becomes larger as Δr_{NORM} becomes smaller. In the second case, increased variation of the fault orientations leads to better sampling of the overlying loading tensor, and r_{CLVD} becomes larger as Δr_{NORM} becomes larger.

APPENDIX D: RELATION BETWEEN DISTRIBUTION OF MINIMUM DC ROTATIONS AND HETEROGENEITY MEASURES

Using the equations of Kagan (2005) we compute the minimum rotation angles Ω_{min} and the rotation axes between all pairs of DC orientations in each of our fault zones for the A and B quality fo-

cal mechanisms. Fig. D1 shows that the average of Ω_{min} correlates with Δr_{NORM} . The measures are not exactly analogous since Ω_{min} measures the orientation difference in 3-D space whereas Δr_{NORM} relates to differences in the space of \hat{P}_{ij} . Fig. D2 shows the orientation density of rotation axes for the minimum rotations and illustrates visually that the distribution is more clustered where $|r_{CLVD}|$ is larger.

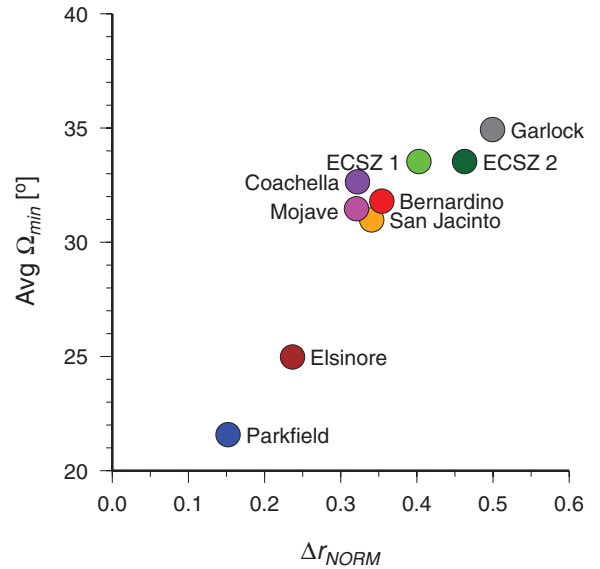


Figure D1. Comparison of heterogeneity for data that sample three kernel densities representing different quality levels in the catalogue. Squares show median values of r_{CLVD} and Δr_{NORM} for the higher quality catalogue, triangles correspond to the lower quality catalogue and circles correspond to the resampled high quality data with a simulated effect of uncertainty. Dashed lines show the changes as lower quality data are included. Error bars show the 75 per cent confidence limits for the bootstrap resampling of r_{CLVD} and Δr_{NORM} which are in many cases smaller than the symbols. We use 75 per cent confidence limits, rather than the minimum and maximum used in Fig. 3 and Fig. B1, to make comparison of values easier.

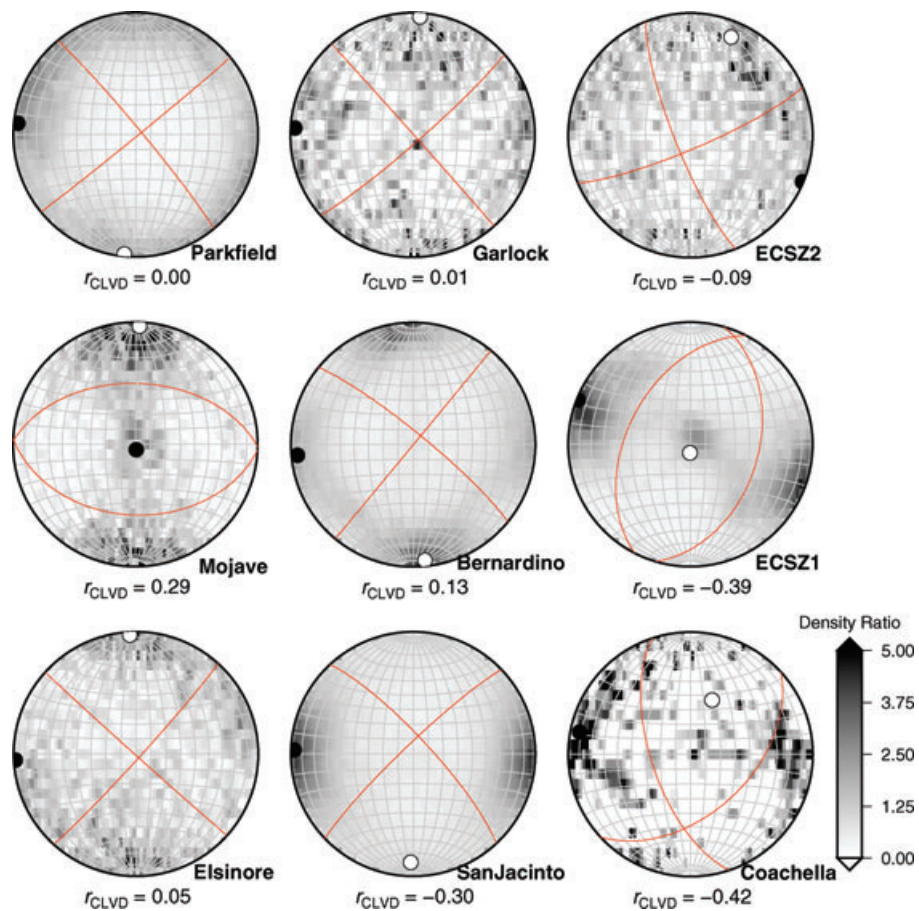


Figure D2. Density of rotation axes orientations for minimum rotations between all DC pairs in the fault zones using equal area lower-hemisphere projections with 5° binning. The density distribution in each case is normalized such that 1 indicates a uniform distribution, but the colour scale is truncated at 5 to allow for comparison. DC orientations for E_{ij} are overlain as red lines, with the P and T axes shown by white and black circles, respectively. The value of r_{CLVD} is given below each of the circles.